Journal of Zhejiang University-SCIENCE A (Applied Physics & Engineering) in press
www.jzus.zju.edu.cn; www.springer.com/journal/11582
E-mail: jzus_a@zju.edu.cn

Research Article

https://doi.org/10.1631/jzus.A2400309

Experimental investigation on the stability of shield tunnel excavation face with water-rich in upper loose and lower dense strata

Pengfei LI[1], Chuang WANG[1], Xiaopu CUI[1]✉, Qing XU[1], Zhaoguo GE[2], Shaohua LI[3]

[1]*Key Laboratory of Urban Security and Disaster Engineering, Ministry of Education, Beijing University of Technology, Beijing 100124, China*
[2]*China Railway 14th Corporation Mega Shield Construction Engineering Co. Ltd., Nanjing 211800, China*
[3]*China Railway 15th Bureau Group Co., Ltd., Shanghai 200070, China*

Abstract: Maintaining the stability of excavation face is key for ensuring the safety of underwater shield tunnel construction. However, the majority of current studies on the stability of excavation face focus on homogeneous strata, with limited research conducted on strata with upper loose and lower dense. Active instability tests are conducted in this study, in concert with the digital image correlation (DIC) technique, to investigate the effects of different water pressure ratios (α) in water-rich upper loose and lower dense strata. The accuracy of these model tests is verified using numerical simulations. The results indicate that as α decreases, there is an increase in both the peak displacement of surface settlement, and the seepage path range of water ahead of the excavation face expands. In contrast, decreasing α will break the limit equilibrium state of the strata faster, cause the earth pressure on the cutterhead to change more rapidly, and increase the instability range of the strata.

Key words: Shield tunnel; Upper loose and lower dense strata; Excavation face stability; Water pressure ratio

1 Introduction

The increasing number of urban transportation projects requires significantly more underwater tunnels. When constructing shield tunnels in water-rich strata, ensuring the excavation face stability is a crucial prerequisite for project success. Currently, studies on excavation face stability which account for the effect of seepage mainly adopt numerical simulation methods, theoretical analysis, and model tests. Due to their reproducibility and flexibility, numerical simulation methods are extensively applied in studying excavation face stability under seepage conditions. These most common of these methods are finite element modeling (Lu et al., 2017; Pan and Dias, 2018; Wang et al., 2019; Ye et al., 2022; Hou et al., 2022; Cheng et al., 2023; Di et al., 2023a) and discrete element methods (Liu et al., 2016; Zhang et al., 2021; Fu et al., 2022; Hou et al., 2023). For example, Li et al. (2023) using numerical simulations and machine learning, established a predictive model for the limit support pressure in the excavation face of an underwater tunnel. Also, Tu et al. (2023) conducted various two-phase single-point material point method simulations, which accounted for the fluid-solid coupling influence to investigate the damage mechanisms of the excavation face in saturated strata.

Since numerical simulation methods need to be validated through model tests or field monitoring, theoretical analytical methods have been adopted by researchers because their derivation can be easily understood. In regard to research on excavation face stability under seepage conditions, theoretical methods are largely concentrated on limit equilibrium methods (Mi and Xiang, 2020a; Han et al., 2021; Huang et al., 2023; Li et al., 2023) and limit analysis methods (Li et al., 2020; Li et al., 2021; Di et al., 2022; Cui et al., 2024). In addition, many scholars have conducted research on excavation face stability for

✉ Xiaopu CUI, cxp2021@emails.bjut.edu.cn
Xiaopu CUI, https://orcid.org/0000-0003-1142-8400

Received June 11, 2024; Revision accepted Aug. 30, 2024; Crosschecked

© Zhejiang University Press 2024

Unedited

saturated strata. By considering the fluid-structure coupling effect, theoretical solutions for the limit support pressure of excavation face under seepage conditions can be derived (Zhang et al., 2022). On the basis of the Hansbo seepage model, Wu et al. (2023) presented a three-dimensional continuity equation for non-Darcy seepage in spherical coordinates.

However, unsaturated strata are also common in the real world. Using the concept of generalized effective stress, Li et al. (2019) obtained the strength of unsaturated soils using an extended form of the Mohr-Coulomb theory, and this provided an effective approach for investigating the effect of unsaturated seepage on excavation face stability. Hou and Yang (2022) proposed a closed form solution characterizing the spatial and temporal variation of saturation, and elucidated the effect of unsaturated transient seepage on the excavation face stability.

For the study of excavation face stability in saturated strata, model tests possess advantages such as convenient observation, controllable formation and boundary conditions, and short testing periods. Model tests are primarily comprised of gravity tests and centrifugal tests. Based on gravity model tests, in which the baffle is made to move backwards, scholars have analyzed the excavation face stability under seepage conditions for sandy soil strata (Lü et al., 2018; Mi and Xiang, 2020b). Centrifugal model tests are also commonly used to investigate the excavation face stability under saturated strata conditions. For instance, Chen et al. (2018) revealed an asymptotic rule for excavation face stability under high hydraulic pressures for sandy silty strata. Moreover, Yin et al. (2021) analyzed the effect of permeability anisotropy on the excavation face stability in sandy silty strata. For clay strata, Weng et al. (2020) concluded that under the assumptions of homogeneous and isotropic soil and steady state seepage flow, the permeability coefficient has no effect on the seepage force in the limit support pressure.

Currently, research on shield tunnel excavation face stability in sandy soil, clay and other strata has made some progress. However, research on excavation face stability in water-rich sandy pebble strata remains scarce (Sohaei et al., 2020; Lei et al., 2021; Jiang et al., 2022). Meanwhile, Di et al. (2023b) concluded that sandy pebble strata with varying degrees of compactness can significantly affect the deformation induced by the excavation face instability. Due to deposition, the actual strata is generally upper loose and lower dense, but most current studies are on sandy pebble strata of uniform compactness (Lin et al., 2021; Di et al., 2023c).

In addition, many studies have been carried out under the assumption that the water pressure of the excavation face is zero. However, in actual engineering, the water pressure is often greater than zero (He et al., 2017; Wan et al., 2022; Di et al., 2024). Therefore, this study is aimed at water-rich sandy pebble strata with upper loose and lower dense. Specifically, we carry out model tests to investigate the active instability under different water pressure ratios α. The variation rules of surface settlement, water pressure, earth pressure on the cutterhead, and earth pressure in the strata with regards to the backward distance L of the baffle are investigated.

2 Engineering background

The Chengdu area is dominated by water-rich sandy pebble strata, and the metro tunnel projects there are influenced by three main characteristics, namely a high water table, high sandy pebble content, and high strength of pebbles and boulders. Therefore, when building shield tunnels in such areas, the excavation face is prone to collapse, after which hidden dangers such as hysteresis settlement will be induced. A shield interval of Chengdu Metro Line 17 has a length of 2802 m, and the depth of the shield tunnel is 15 m. The shield tunnel lining has an outer diameter of 7.5 m and an inner diameter of 6.7 m. The width of the segment is 1.5 m and its thickness is 0.4 m. The shield tunnel passes under the Jiang'an River (a source of major hazards) within the area of the interval, and the distance between the river bottom and the tunnel top is about 15m.

The strata in this area are mainly of sandy pebble type, except for a small amount of miscellaneous fill in the upper part. The strata from top to bottom are the slightly dense sandy pebble stratum, the medium dense sandy pebble stratum, and the dense sandy pebble stratum. The codes of three strata are I, II, and III, respectively. The specific parameters of the strata are given in Table 1.

Unedited

Table 1 Measured data of the experiments in five states.

Stratum code	Buoyant unit weight γ' (kg/m^3)	Internal friction angle φ (°)	Young's modulus E (MPa)	Poisson's ratio μ	Relative compactness D_r	Cohesion c (kPa)
I	1900	38	18	0.27	0.33	0
II	2100	42	38	0.24	0.57	0
III	2300	45	50	0.22	0.78	0

The shield machine mainly operates in the demarcation between medium dense sandy pebbles and dense sandy pebbles, as illustrated in Fig. 1. Therefore, the strata ahead of the excavation face in this model test is in the form of intermediate stratification.

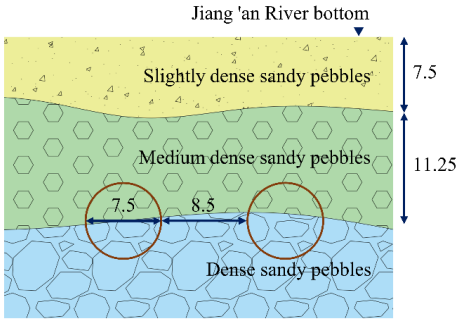

Fig. 1 Geographic profile. Units: m.

3 Model test designs

3.1 Similar strata designs

The diameter of the shield tunnel in the Chengdu Metro Line 17 tunnel project is 7.5 m, and the diameter of the shield tunnel in the test model is D = 300 mm. Thus, the geometric similarity ratio between the model test and the actual project is 1:25. When formulating the similar soil material in the model test, the ideal similarity ratio is 1:1, accounting for the similarity of the density of gravity and internal friction angle. The cohesion and internal friction angle of the three similar soils are derived by a straight shear test; these results for each stratum are illustrated in Fig. 2.

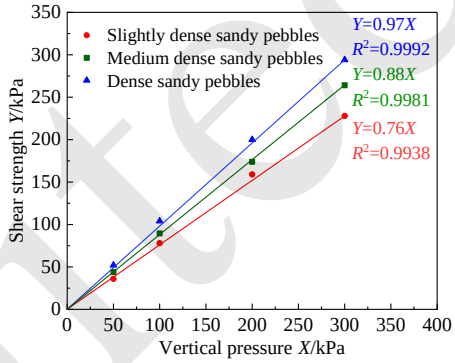

Fig. 2 The results of straight shear tests.

From three fitted straight lines, the internal friction angles of the three similar strata are respectively 37.3°, 41.4°, and 44°, and their cohesion is 0 kPa. The density of the fill corresponding to the three similar strata is obtained from the relative compactness test, with the values of the specific parameters being illustrated in Table 2.

Table 2 Physical and mechanical parameters of the strata.

Stratum code		Relative compactness D_r	Buoyant unit weight γ' (kg/m^3)	Thicknesses h (m)	Internal friction angle φ (°)
I	prototype	0.33	1900	7.5	38
	model	0.35	1950	0.3	37.3
II	prototype	0.57	2100	11.25	42
	model	0.55	2130	0.45	41.4
III	prototype	0.78	2300	-	45
	model	0.75	2340	0.35	44

3.2 Test device

The shield tunnel excavation seepage stability model test device is illustrated in Fig. 3, and consists of a model box, a tunnel model, an excavation face control system, a tunnel-pump-surface water circulation system, and a data measurement and acquisition system (Mi and Xiang, 2020b). This model test device is used for investigating shield tunnel excavation face stability in water-rich sandy pebble strata with upper loose and lower dense, for different excavation face water pressure ratios (α = 1, 0.5, and 0). The water pressure ratio α is determined by the following equation:

Unedited

$$\alpha=\left(h_w+D-\Delta\right)/\left(h_w+D\right). \quad (1)$$

Here, h_w is the distance from the tunnel top to the water level, D is the diameter of the tunnel, and Δ is the difference between the water ahead of the excavation face and the surface water head.

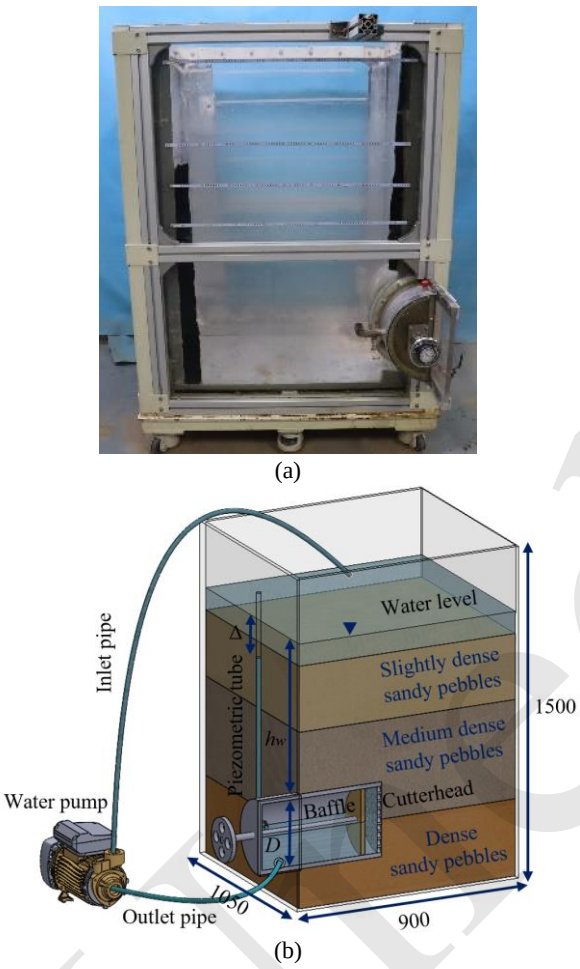

Fig. 3 The shield tunnel excavation seepage stability model test device: (a) Picture of the model box; (b) Diagrammatic drawing of the model box. Units: mm.

The interior of the model box has a length of 900 mm, a width of 1050 mm, and a height of 1500 mm. The tunnel model is cut from an aluminum cylinder with a length of 400 mm, an inner diameter of 300 mm, and a thickness of 20 mm, with a semi-circular cross-section.

The excavation face control system consists of a cutterhead and a baffle that can simulate the shield excavation chamber. The cutterhead is made of a 20 mm-thick semi-circular plastic plate with evenly-cut holes. The baffle is made of a combination of semi-circular sponge and steel wire mesh, so that water can pass through the baffle but soil cannot. The baffle is connected to a rotating wheel by a bearing. The cutterhead with evenly-cut holes is fixed, and the baffle can be moved backward horizontally. During the test, the baffle is moved backward by turning the wheel counterclockwise. The support pressure of the excavation face is insufficient, thus causing active instability of the excavation face.

The bottom and back sides of the model box are made of 5 mm-thick steel plates. The front, left, and right sides of the model box are made of 20 mm-thick transparent acrylic glass panels, used as observation windows.

3.3 Monitoring schemes

Sixteen settlement monitoring points are placed on the surface of the strata model, as illustrated in Fig. 4. Surface displacement data is acquired by static strain collector.

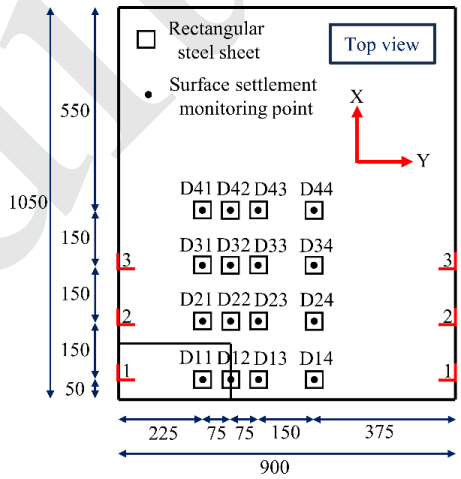

Fig. 4 Distribution of surface settlement monitoring points. Units: mm.

Twenty-three vertical earth pressure boxes are placed in the strata, as illustrated in Fig. 5. The earth pressure box has a diameter of 28 mm and a thickness of 7 mm, which enables functionality in saturated soil. Monitoring data of earth pressure in the strata is also acquired by static strain collector.

Unedited

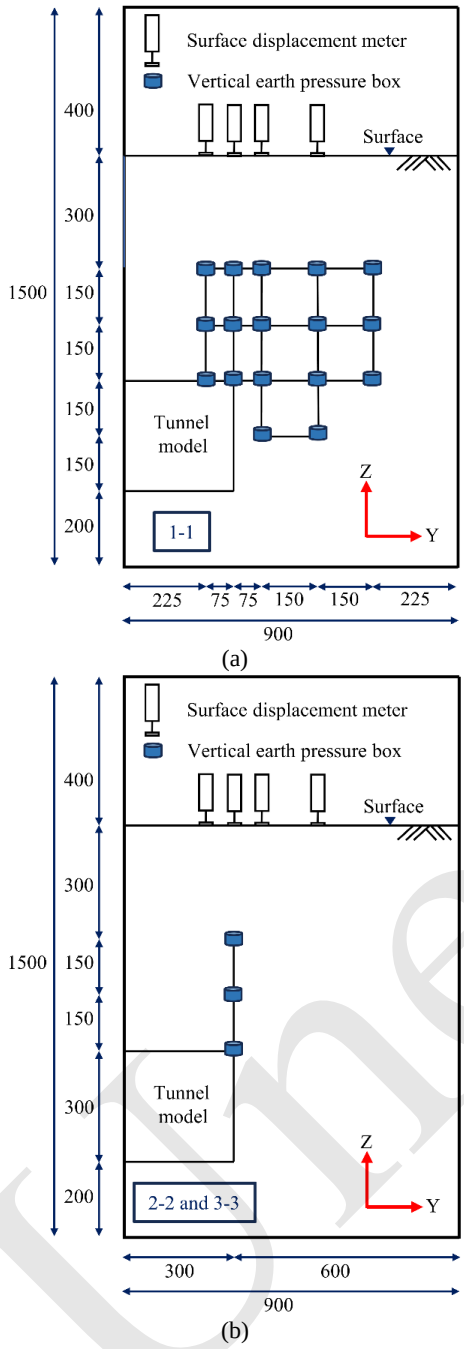

Fig. 5 Distribution of earth pressure boxes in the strata: (a) 1-1 section; (b) 2-2 and 3-3 section. Units: mm.

Six earth pressure boxes are placed on the cutterhead, and five osmometers are placed on the axis of the tunnel and fixed on the acrylic plate of the model box, as illustrated in Fig. 6. The monitoring data of water pressure is acquired by osmometer collector.

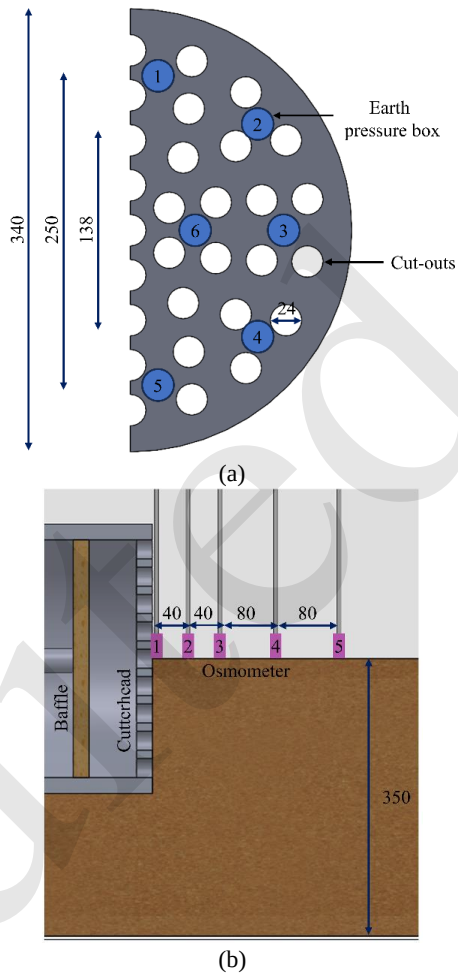

Fig. 6 Distribution of earth pressure boxes and osmometers: (a) Distribution of earth pressure boxes on the cutterhead; (b) Distribution of osmometers ahead of the excavation face. Units: mm.

3.4 Testing procedure

The specific testing procedure is illustrated in Fig. 7, and the steps are as follows:

(1) The model box is first cleaned, and then the inside of the box is coated with petroleum jelly to reduce friction.

(2) The mass of model soil required for sandy pebbles with different degrees of compactness is calculated. Then soil is filled to a predetermined height, according to the set mass. During the filling process, earth pressure boxes are buried at predesignated locations. When the height is 350 mm, the soil is leveled and colored sand is laid. Then colored sand is laid at 100 mm intervals, starting at a height of 500 mm. After each 10 cm thickness of soil is filled, water is sprayed by a sprinkler to make the water overflow the soil surface. After waiting for a

Unedited

period of time, the water level does not drop and there is no air bubble above the soil, indicating that the soil is saturated.

(3) When the strata reaches a height of 1100 mm, the surface is leveled and the surface displacement meter is set up. Then a water sprinkler is used to bring the water level up to 1200 mm. At the same time, the static strain collector, the osmometer collector, and the digital image correlation (DIC) equipment are connected.

(4) The baffle is moved backward at a rate of 0.1 mm/s by rotating the wheel. In the whole test process, the height of the water column in the piezometric pipe under different α conditions is controlled by the water pump valve. After every 1 mm of movement, we wait until all measurements have stabilized, and then continue to move backwards. The backward distance of the baffle is represented by L. When L = 10 cm, the test is completed.

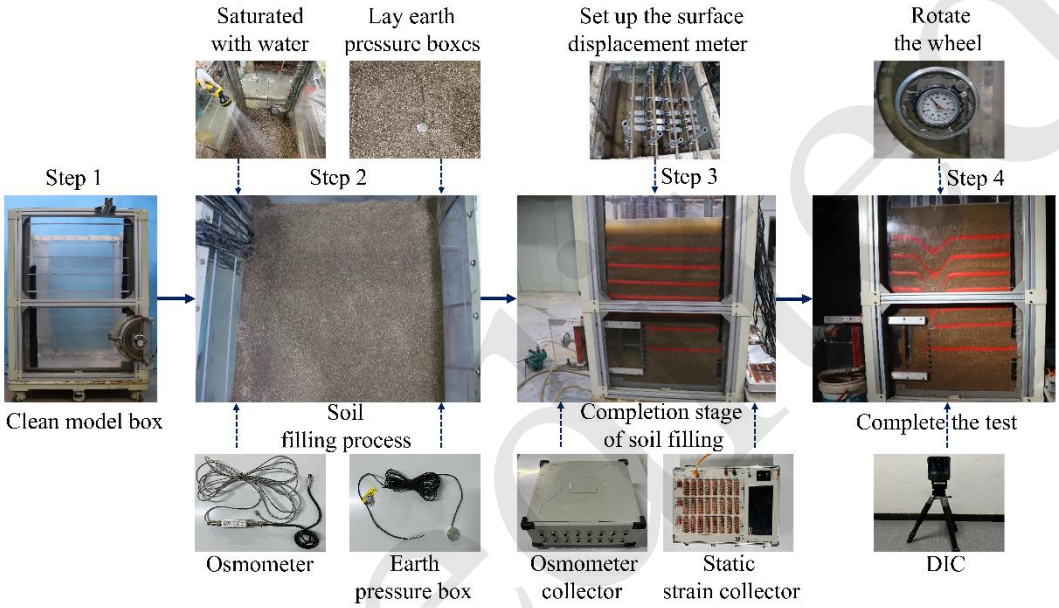

Fig. 7 Testing procedure.

3.5 Establishing the numerical model

In order to validate the model tests, numerical simulations are carried out under different α conditions using the *ABAQUS* software. The model of water-rich sandy pebble strata with upper loose and lower dense is illustrated in Fig. 8. The dimensions of the numerical simulation are consistent with the dimensions of the model test, and the soil parameters in the numerical simulation are essentially consistent with those of the test soil. The permeability coefficient k of the soil in the numerical simulation is measured from the constant head permeability test, with $k = 2 \times 10^{-5}$ m/s.

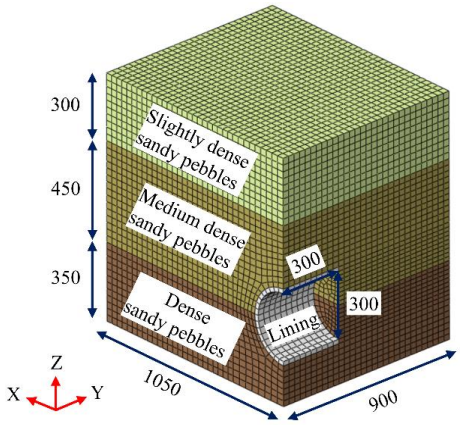

Fig. 8 Numerical model. Units: mm.

Since our analysis focuses on the stability of the excavation face, a simplified single-step (300 mm) excavation scheme is adopted. According to Eq. (1), the water head of the excavation face is set for different α values. For α = 1, the excavation face is set to be a free permeable interface, and the water pressure

at each position ahead of and behind the excavation face is set as equal. For α = 0.5, the water head of the excavation face is set to 5000 Pa. For α = 0, the water head of the excavation face is set to be a completely free permeable interface, and the water head of the excavation face is set to 0.

The numerical simulation process is as follows.

(1) A numerical model of the same dimensions as the model test is established. The portion representing the tunnel is set to be an empty unit, and the lining unit is set to support the tunnel. The material properties are defined and the boundary conditions are set, and then the initial geostress balance is calculated.

(2) The speed of the excavation face moving back along the normal direction is set to 0.002 mm/iteration step, and the fluid-structure coupling calculation is carried out. The constraint condition of the excavation face is changed to be a normal fixed constraint for each 1 mm backward movement, and then the fluid-structure coupling calculation is carried out to the equilibrium state.

(3) The above process is repeated, and the numerical simulation is completed when the excavation face moves backwards by 10 cm.

4 Engineering background

Model tests are carried out under different α conditions, with the test results illustrated in Figs. 9–11 for L = 10 cm.

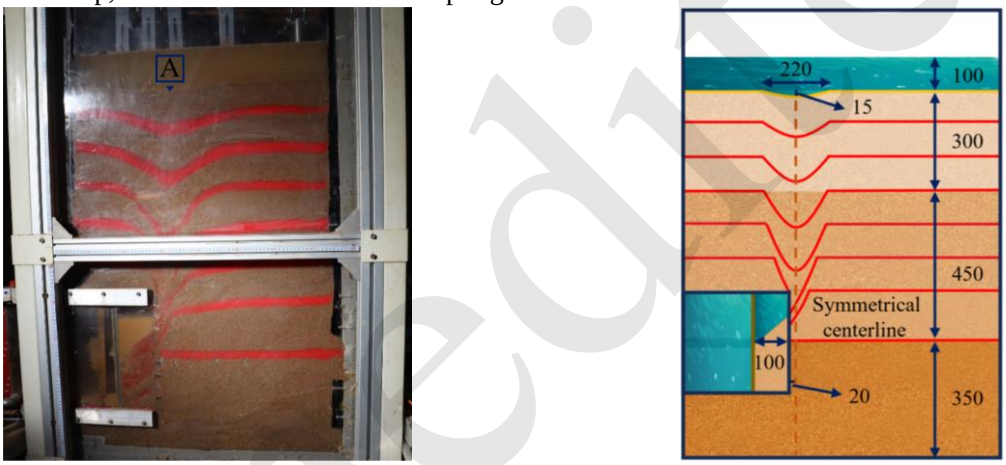

(a) (b)

Fig. 9 α = 1: (a) Picture the test result; (b) Diagram of the test result. Units: mm.

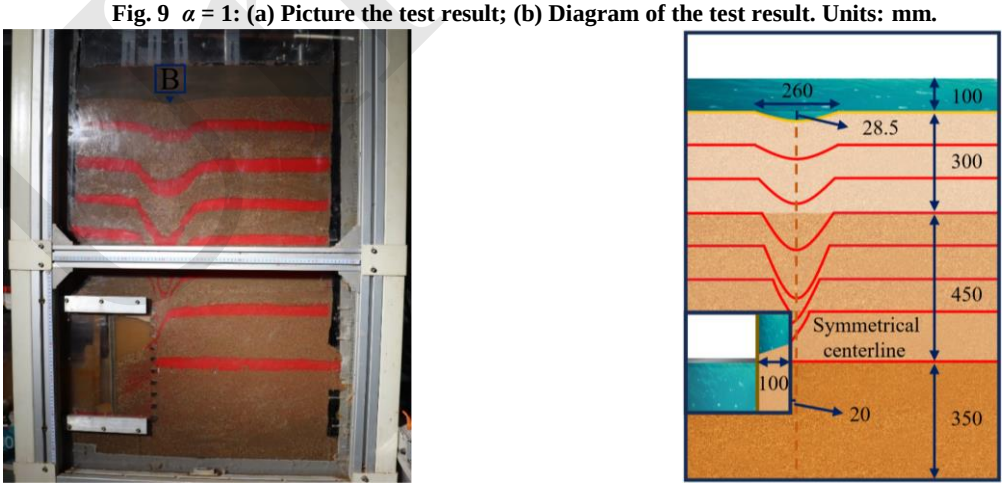

(a) (b)

Fig. 10 α = 0.5: (a) Picture the test result; (b) Diagram of the test result. Units: mm.

Unedited

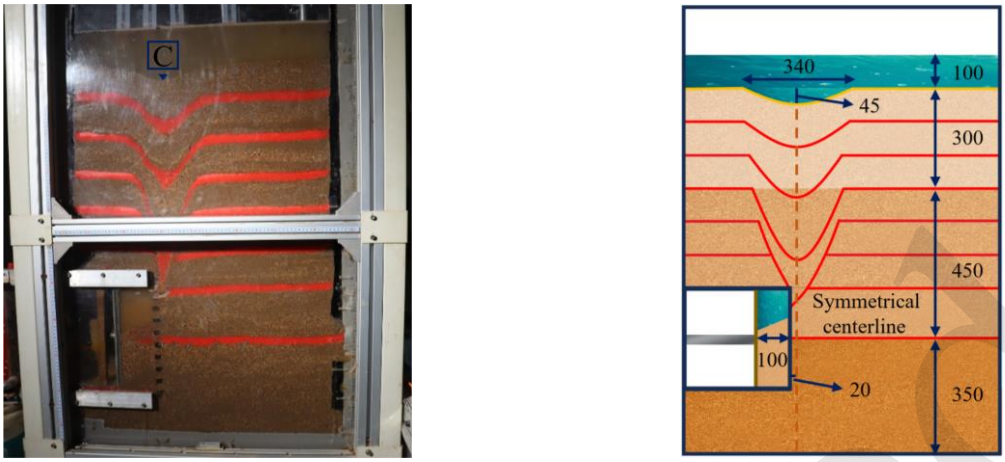

(a) (b)

Fig. 11 α = 0: (a) Picture the test result; (b) Diagram of the test result. Units: mm.

4.1 Model test and numerical simulation validation

The variation rule of surface settlement is analyzed using the DIC technique, and the soil displacement incremental field in front of the excavation face for different α values is obtained, as illustrated in Fig. 12.

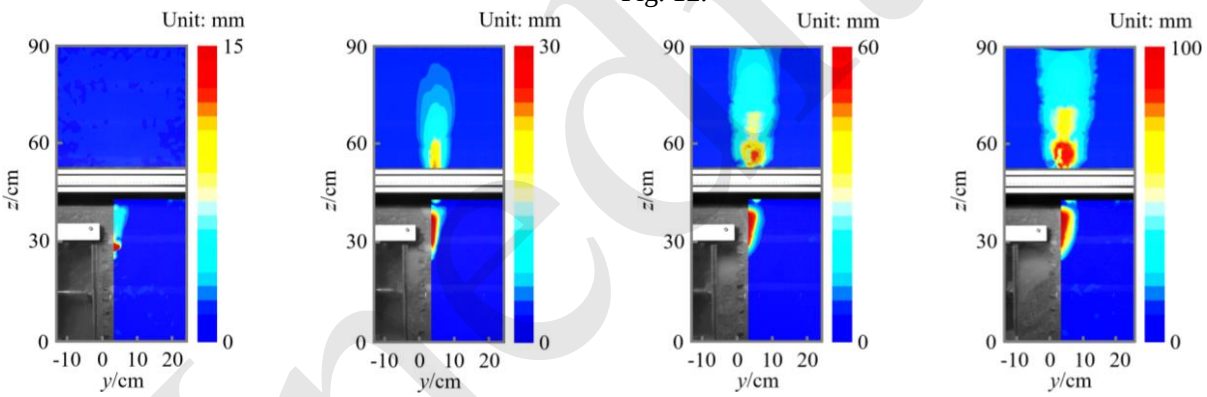

(a)

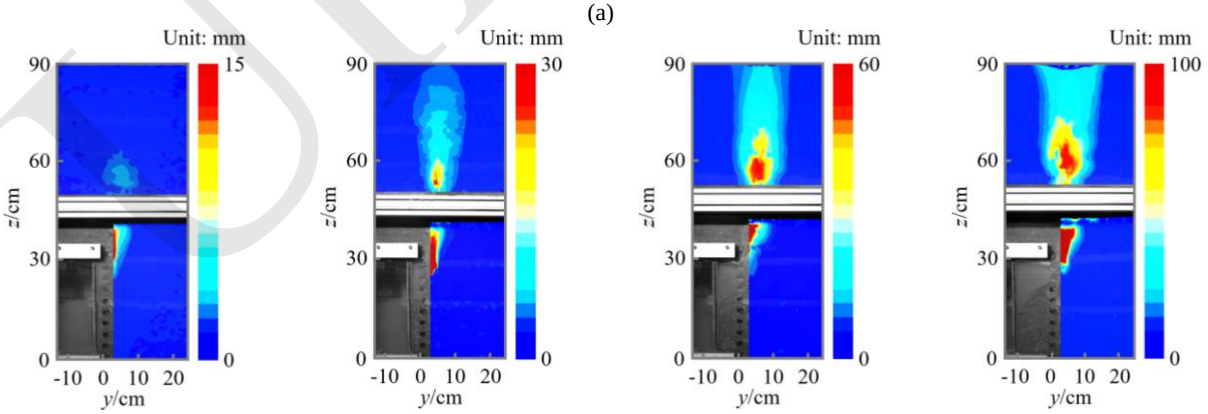

(b)

Unedited

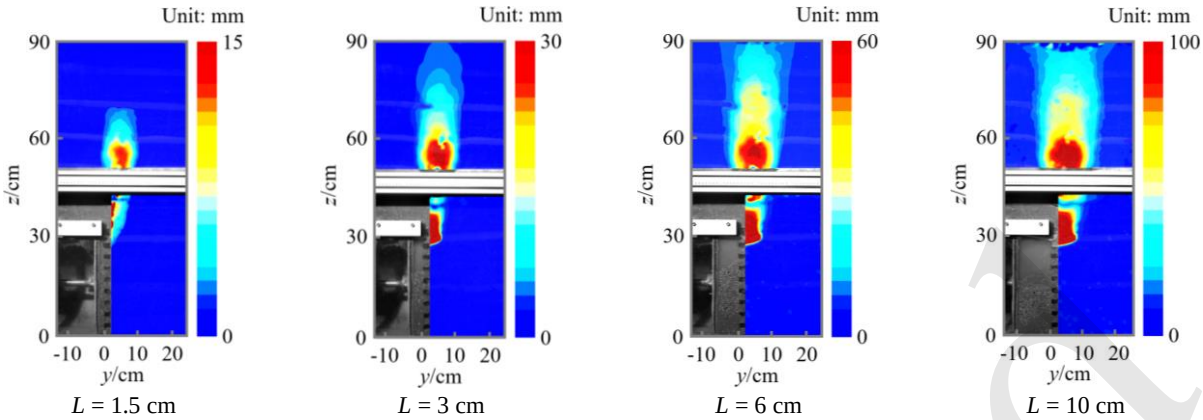

(c)

Fig. 12 The soil displacement incremental field for different α values: (a) α = 1; (b) α = 0.5; (c) α = 0.

Fig. 13 presents the variation rule of the peak displacement of surface settlement with L, and we analyze the results of the model tests and numerical simulations simultaneously. In the model tests, the locations of the peak displacement of surface settlement for different α values are at points A, B, and C respectively, as illustrated in Figs. 9–11. In the numerical simulation, the locations of the peak displacement of surface settlement for different α values are also defined as points A, B, and C.

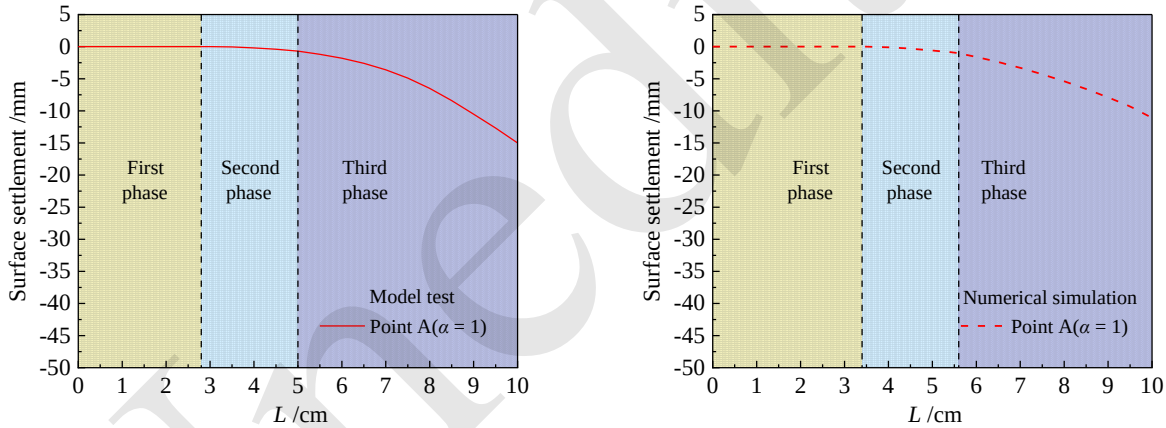

(a)

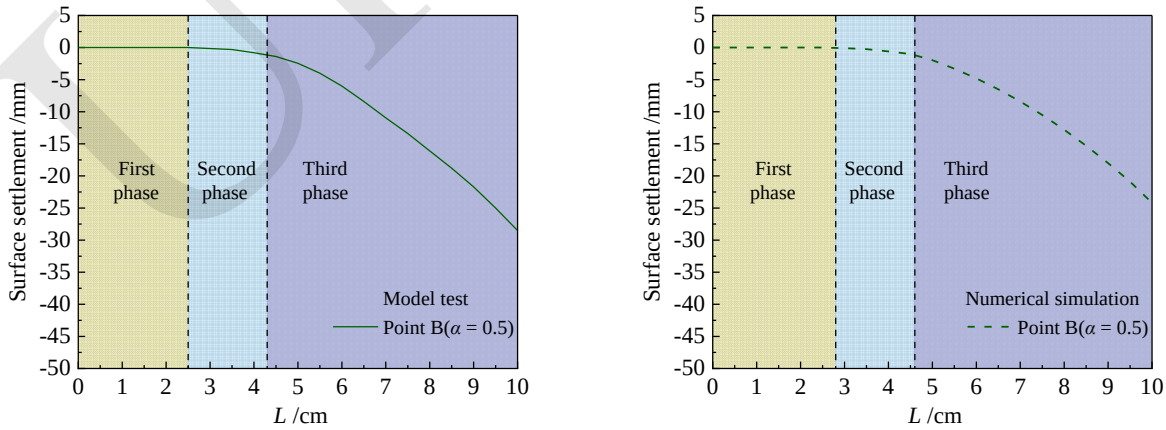

(b)

Unedited

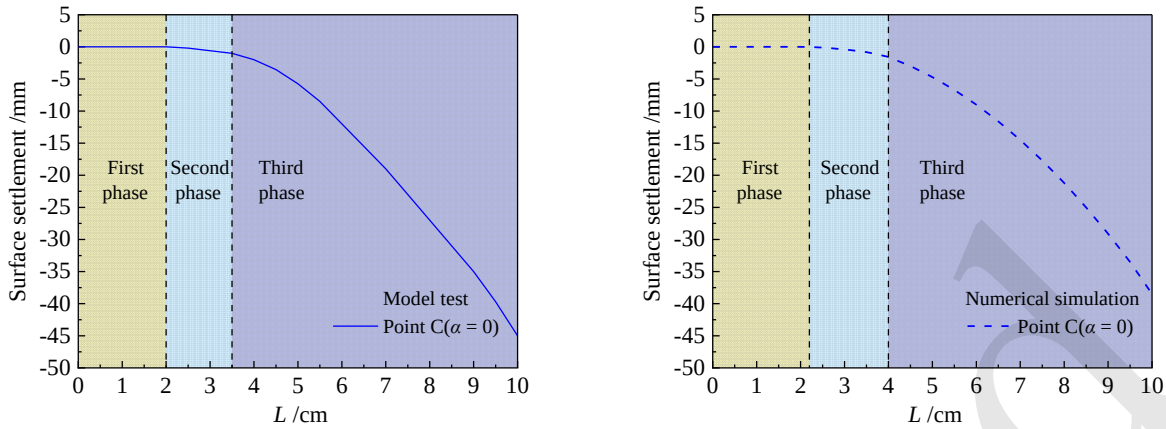

(c)

Fig. 13 The variation rule of peak displacement of surface settlement with *L*: (a) *α* = 1; (b) *α* = 0.5; (c) *α* = 0.

For both the model tests and numerical simulations, it is found that under different α conditions, the variation rule of peak displacement of surface settlement is categorized into three phases. The range of L corresponding to the three phases for different α values are shown in Table 3.

Table 3 The range of *L* at each phase for different *α* values.

Test condition		*L* (cm)		
		First phase	Second phase	Third phase
Model test	$\alpha = 1$	0-2.8	2.8-5	5-10
	$\alpha = 0.5$	0-2.5	2.5-4.3	4.3-10
	$\alpha = 0$	0-2	2-3.5	3.5-10
Numerical simulation	$\alpha = 1$	0-3.4	3.4-5.6	5.6-10
	$\alpha = 0.5$	0-2.8	2.8-4.6	4.6-10
	$\alpha = 0$	0-2.2	2.2-4	4-10

(1) Non-displacement phase. As the baffle moves backwards, the support pressure acting on the excavation face is reduced, which leads to active instability of the strata. At this phase, the soil arch begins to form and develop, but it does not reach the surface.

(2) Slow descent phase. When the soil arch gradually develops to the surface, the instability range gradually increases, but the surface settlement increases slowly. At this stage, we mainly see that the influence of L is to increase the instability range of the strata.

(3) Rapid descent phase. With the increase of L, the soil arch effect gradually disappears, and overall instability of the strata occurs. The instability range of the strata increases slowly, and the surface settlement develops rapidly. At this phase, the influence of L is mainly to increase the settlement of the strata. With the decrease of α, the peak displacement of surface settlement gradually increases for a given L.

With the decrease of α, overall instability of the strata in the model tests occurs at L values of 5 cm, 4.3 cm, and 3.5 cm, and in the numerical simulations, the overall instability of the strata occurs at L values of 5.6 cm, 4.6 cm, and 4 cm. Meanwhile, under the same α and L conditions, the peak displacement of surface settlement obtained from the numerical simulations is smaller than that obtained from the model tests. This indicates that the stability of the strata in the numerical simulations is slightly greater than the stability in the model tests. This is primarily due to the fact that the numerical simulations use continuous strata units, whereas the particles of strata in the model tests are discrete.

4.2 Three-dimensional surface settlement analysis

When L = 10 cm, the surface settlement is obtained from 16 surface displacement meters, and the three-dimensional surface settlement is fitted for different α, as illustrated in Fig. 14.

Unedited

This analysis indicates that a symmetrical semi-funnel-shaped settlement is produced at the surface after completion of the test. Its symmetrical centerline is located about 2 cm ahead of the vertical line corresponding to the excavation face. With the decrease of α, the maximum radius of the funnel gradually increases to 11 cm (0.367D), 13 cm (0.433D), and 17 cm (0.567D). Meanwhile, the maximum settlement of the funnel increases gradually as α decreases, with values of 15 mm, 28.5 mm, and 45 mm. These conclusions are consistent with those obtained by DIC analysis.

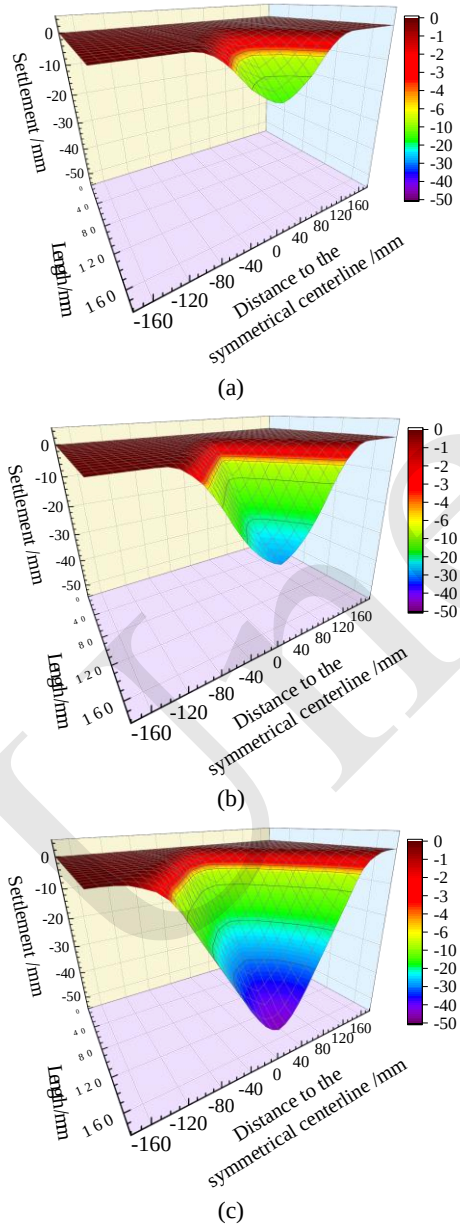

Fig. 14 Three-dimensional surface settlement: (a) α = 1; (b) α = 0.5; (c) α = 0.

4.3 Water pressure analysis

Due to the condition that α = 1 does not adjust the water pump valve, the chamber is always full of water as the baffle moves backwards. Additionally, the water pressure in front of and behind the excavation face is equal, and it can be considered that no seepage occurs on the excavation face. Therefore, under the conditions that α = 1, the seepage field is steady throughout the test, and the water pressure in each osmometer remains level.

Under the conditions that α = 0.5 and α = 0, the variation rule of water pressure ahead of the excavation face with L is illustrated in Fig. 15.

Except for Osmometer 5, which leaves the excavation face furthest under the α = 0.5 condition, the water pressure at each osmometer tends to increase and later stabilize as L increases. This is because before starting the test in these two working conditions, water needs to be released to the set position in the chamber. With the increase of L, the seepage gradually becomes stable.

Under the condition that α = 0.5, the seepage path is within the range of 0-16 cm (0-0.53D). Under the condition that α = 0, the seepage path is within the range of 0-24 cm (0-0.8D).

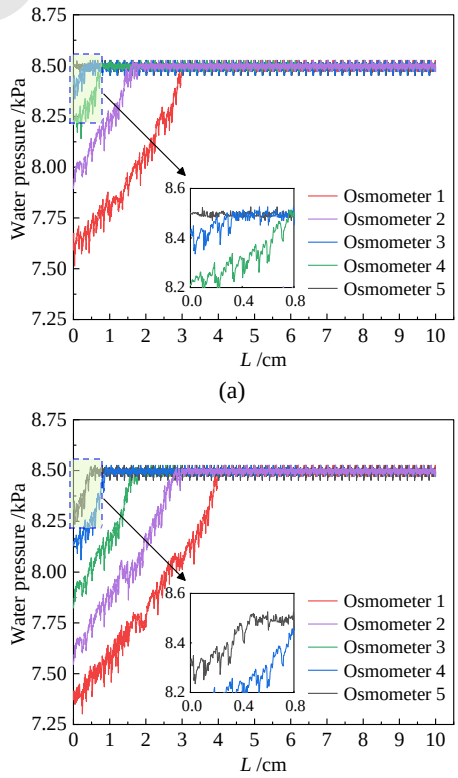

Unedited

Fig. 15 The variation rule of water pressure with L: (a) α = 0.5; (b) α = 0.

Next, we compare the seepage path range obtained from the numerical simulations with that obtained from the model tests. Under different α conditions, the pore pressure distribution and seepage velocity of the strata are illustrated in Figs. 16–17. When α = 1, the water pressure ahead of and behind the excavation face is the same, which is equivalent to the situation without seepage. Therefore, the range of seepage field under the conditions of α = 0.5 and α = 0 is analyzed below.

It is clear that the water in the strata flows towards the tunnel area, and the far boundary remains at hydrostatic pressure. Under the condition that α = 0.5, the seepage path is within the range of 0-0.46D in the numerical simulation. Under the condition that α = 0, the seepage path is within the range of 0-0.72D in the numerical simulation. This analysis shows that the range of seepage path increases with the decrease of α, which is consistent with the results of the model tests.

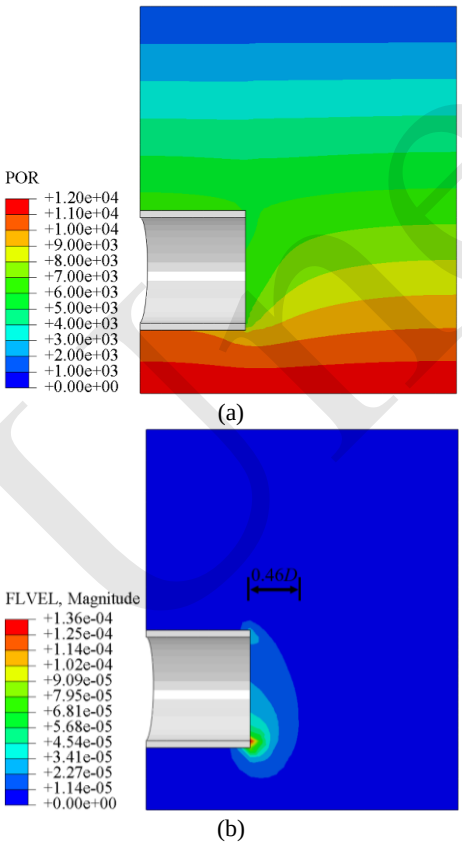

Fig. 16 The pore pressure distribution and seepage velocity for α = 0.5: (a) Pore pressure distribution; (b) Seepage velocity.

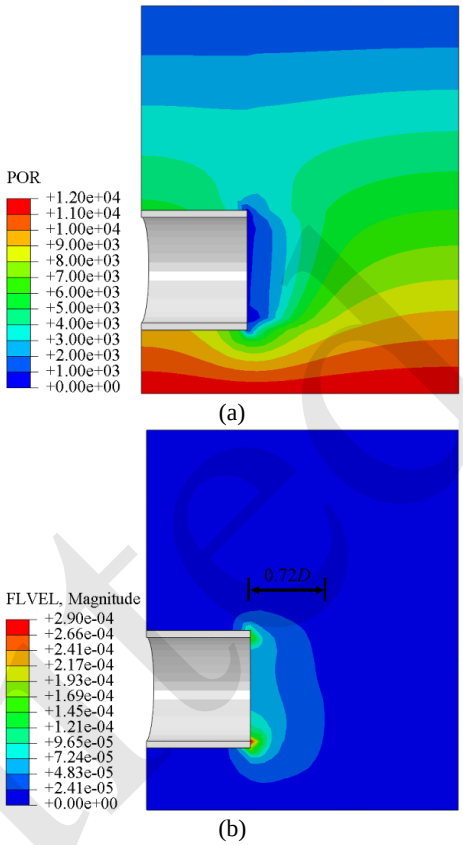

Fig. 17 The pore pressure distribution and seepage velocity for α = 0: (a) Pore pressure distribution; (b) Seepage velocity.

The results of the model tests and numerical simulations show that the seepage path range of water will increase with the decrease of α. Moreover, the water pressure is high ahead of the excavation face and low behind the excavation face. Water will thus flow from a high-pressure region to a low-pressure region, creating the seepage force. For constant L, as α decreases, the water pressure difference between the front and back of the excavation face gradually increases, so the seepage force gradually increases. Therefore, the decrease of α will cause the water to carry more soil particles into the chamber, resulting in a larger instability range of the strata.

4.4 Earth pressure analysis

4.4.1 Earth pressure analysis on the cutterhead

The amount of change in earth pressure on the cutterhead for varying L values is illustrated in Fig. 18. Under different α conditions, each soil pressure presents the same variation rule with the increase of L.

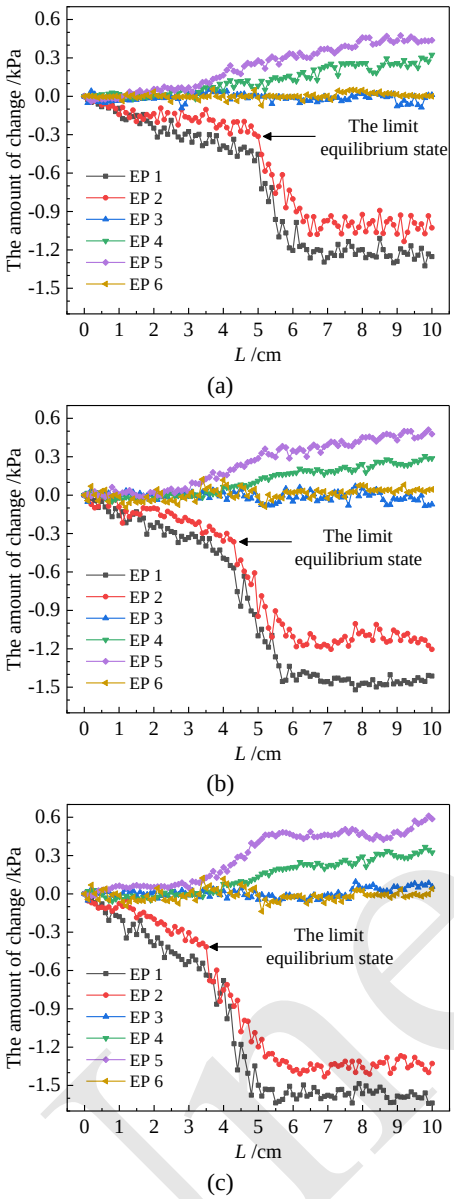

Fig. 18 The amount of change in earth pressure on the cutterhead with *L*: (a) *α* = 1; (b) *α* = 0.5; (c) *α* = 0.

No. 3 and No. 6 earth pressure boxes are fixed in the center of the cutterhead, and their earth pressures EP 3 and EP 6 are basically unaffected during the entire test process. Looking at Figs. 9–11, the colored sand at 350 mm is not disturbed, which also verifies this conclusion. No. 4 and No. 5 earth pressure boxes are fixed at the lower part of the cutterhead, and their earth pressure EP 4 and EP 5 gradually increase. This is because the soil continues to enter the chamber, and the earth pressure boxes below are subjected to the squeezing action.

The earth pressure EP 1 and EP 2 show a trend of slowly decreasing, then rapidly decreasing and finally stabilizing. This is due to the backward movement of the baffle, which leads to active instability of the soil ahead of the excavation face. The soil continuously enters the chamber through the cut-outs in the upper part of the cutterhead, resulting in a gradual decrease of the surrounding earth pressure. With the continuous increase of L, the limit equilibrium state of the strata is broken. A small reduction of the support pressure will lead to a large amount of soil collapse, and the earth pressure EP 1 and EP 2 drop rapidly accordingly. Finally, stable seepage flow is formed in the strata, and the earth pressure on the cutterhead is also stable. One can observe that with the decrease of α, the corresponding L values in the limit equilibrium state decrease, which are 5 cm, 4.3 cm, and 3.5 cm.

At the same time, for constant L, the change in EP 1 and EP 2 involves a gradual increase with the decrease of α. This is due to the decrease of α, which leads to the increase of seepage force ahead of excavation face. Water will carry more soil particles into the chamber, thus increasing the degree of change in earth pressure within the disturbed range. When L = 10 cm, the amounts of decrease in EP 1 are 1.25 kPa, 1.41 kPa, and 1.64 kPa, and the amounts of decrease in EP 2 are 1.03 kPa, 1.20 kPa, and 1.33 kPa. These show that the decrease of α will lead to greater changes and a more rapid change of the earth pressure on the cutterhead, which will cause overall instability and displacement of the strata in advance.

4.4.2 Earth pressure analysis in the strata

In order to more directly reflect the variation rule of the earth pressure in the strata, the ratio of the vertical earth pressure under different L to its initial value is defined as n_{sx}. Meanwhile, in order to study the failure model of the excavation face, the instability range of the strata is obtained from the DIC analysis, as illustrated in Fig. 22.

The variation rules of the coefficient n_{sx} parallel and perpendicular to the excavation face direction are illustrated in Figs. 19–21. When L is at different positions, the variation of n_{sx} reflects the disturbed range of vertical earth pressure. Under the condition that α = 1, the disturbed length of the vertical earth pressure is less than 1D, and the disturbed width of the vertical earth pressure is less than 0.5D. Compared to the condition that α = 1, the disturbed range of vertical

Unedited

earth pressure increases under the condition that α = 0.5. But the disturbed length is also less than 1D and the disturbed width is also less than 0.5D. Under the condition that α = 0, the disturbed length is more than 1D, and the disturbed width is more than 0.5D. With the decrease of α, the disturbed range of earth pressure in the strata increases. This also indicates that the decrease of α will lead to the expansion of the instability range and surface settlement.

The vertical earth pressure in front of the excavation face is significantly more disturbed than the pressure behind. Because the baffle moves backwards, the soil ahead of the excavation face enters the chamber first. Furthermore, there are vertical earth pressure boxes located in front of the center of the tunnel, whose n_{sx} is essentially equal to 1, indicating that they are unaffected by L. From Fig. 22, one can observe that the instability range ahead of the excavation face is larger than that behind the excavation face, and the dense sandy pebbles stratum is unaffected by the strata instability.

Meanwhile, the vertical earth pressure at different locations in the disturbed range tends to decrease gradually with the increase of L, and this rule becomes increasingly pronounced as α decreases. In Fig. 22 the instability range of the strata has been plotted, abstracting the instability range into three-dimensional geometry. Under different α conditions, with the decrease of n_{sx}, the soil arch begin to form and develop, but it does not affect the surface. At the same time, the instability range of the strata develops from the "quarter ellipsoid" model to the "quarter ellipsoid + circular truncated cone + semiellipsoid" model. When α = 0.5 or 0, the soil arch develops rapidly. When L = 1.5 cm in Fig. 22 (b) and Fig. 22 (c), the instability range develops into the "quarter ellipsoid + circular truncated cone + semiellipsoid" model. Later, with the further decrease of n_{sx}, the soil arch effect reaches the surface and gradually disappears. The overall instability of the strata therefore manifests, and the failure model of "quarter ellipsoid + circular truncated cone + cylinder + circular truncated cone" forms.

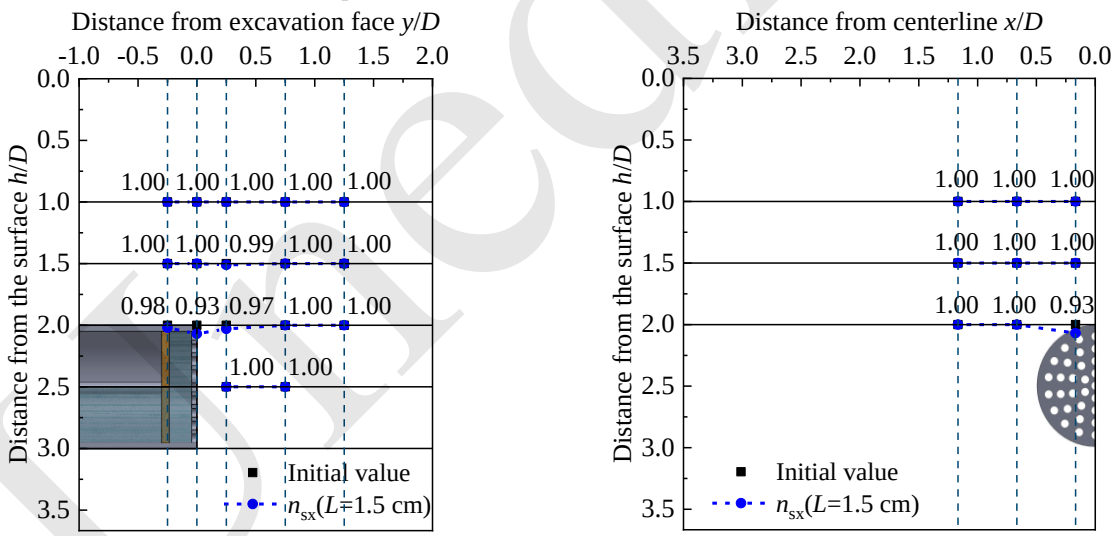

(a)

Unedited

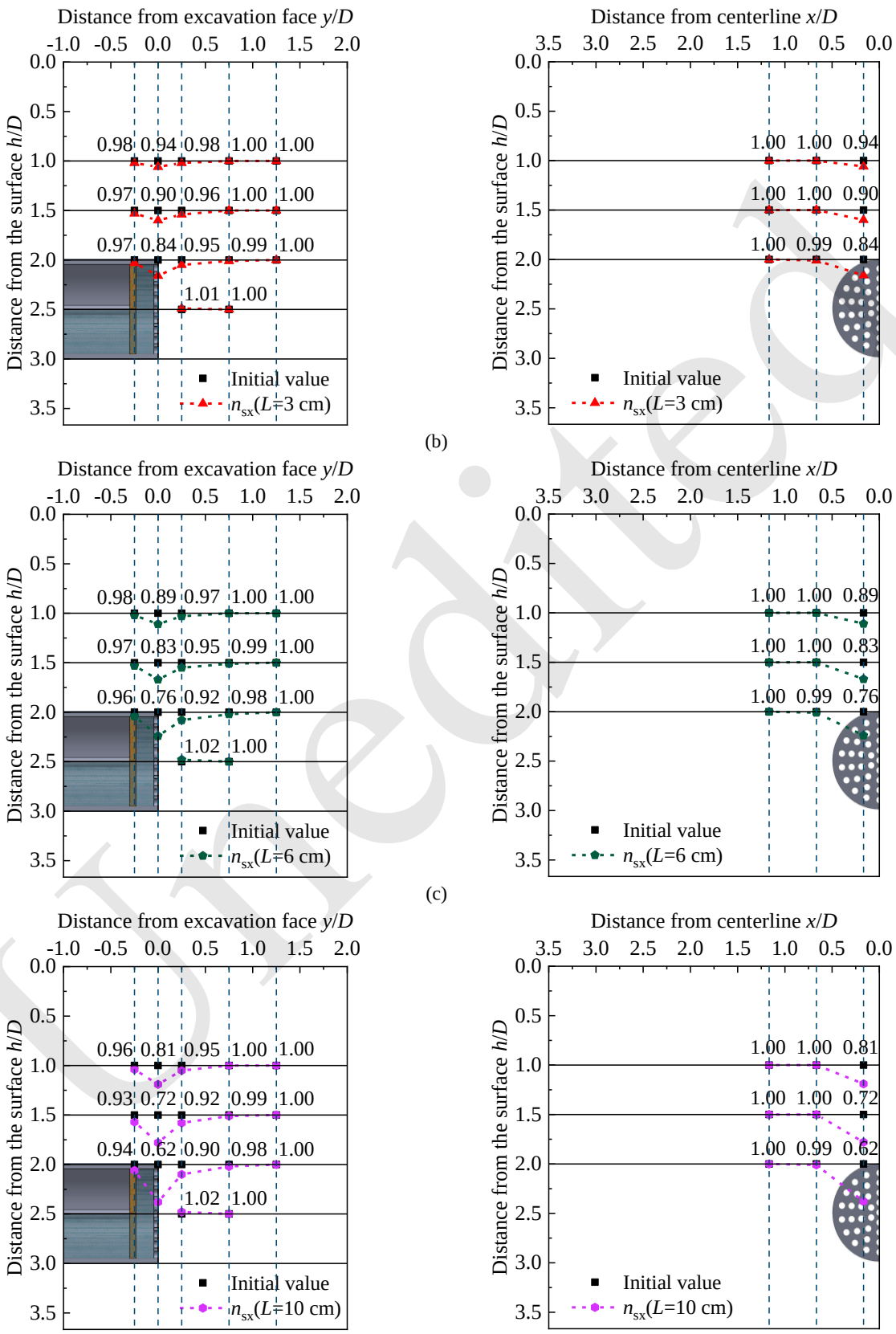

Fig. 19 The variation rule of n_{sx} with L when α = 1: (a) L = 1.5 cm; (b) L = 3 cm; (c) L = 6 cm; (d) L = 10 cm.

Unedited

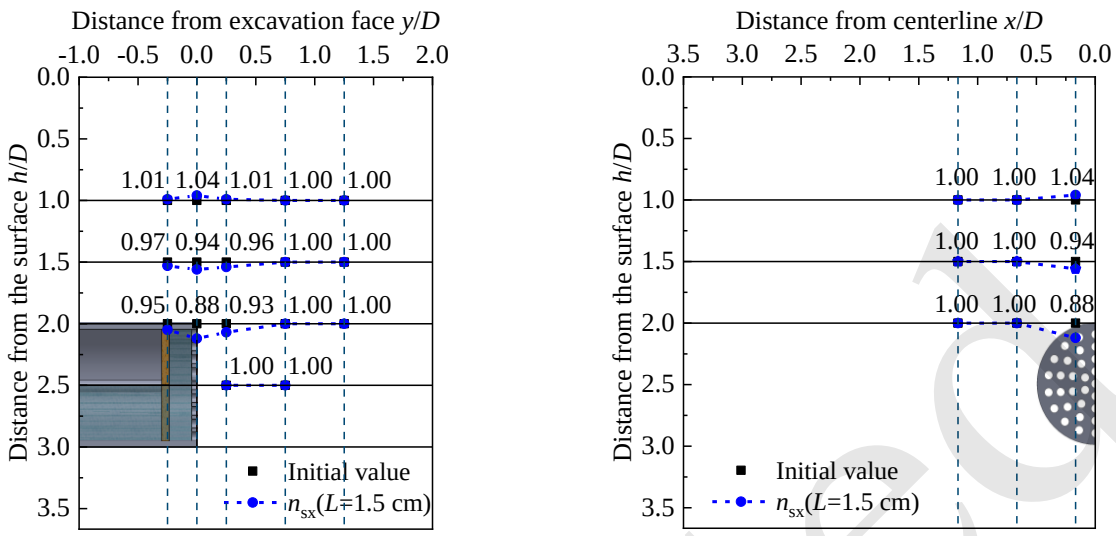

(a)

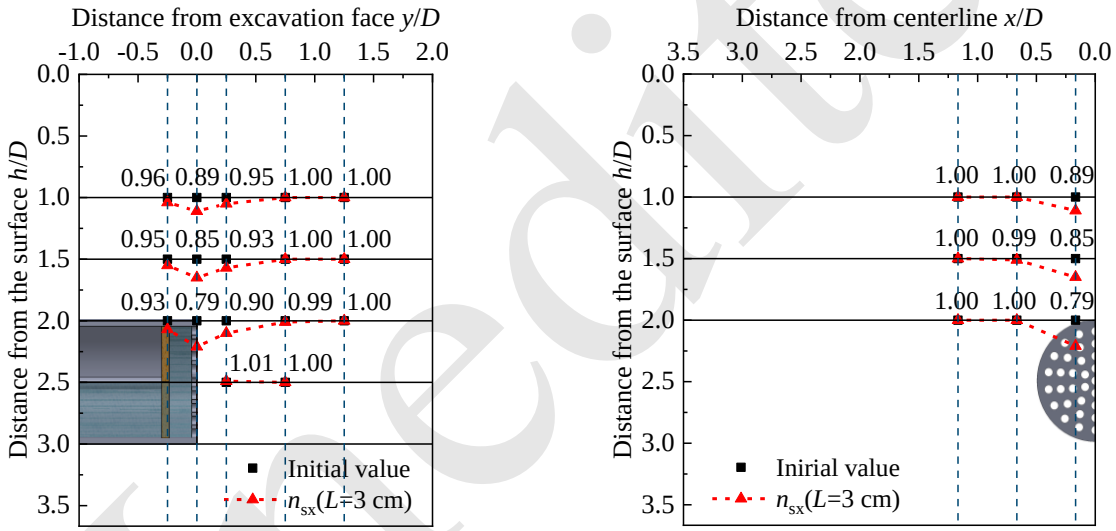

(b)

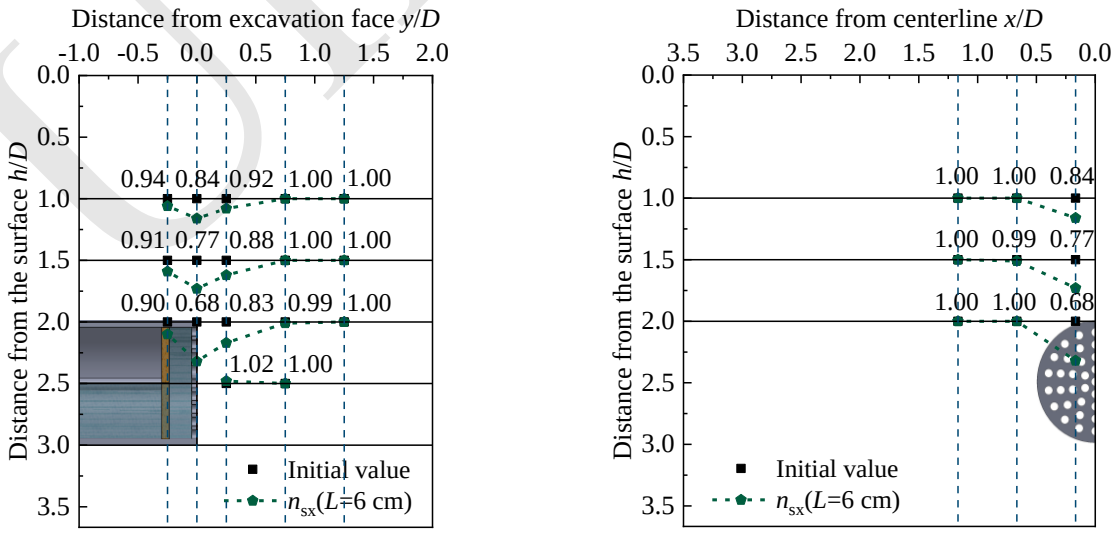

(c)

Unedited

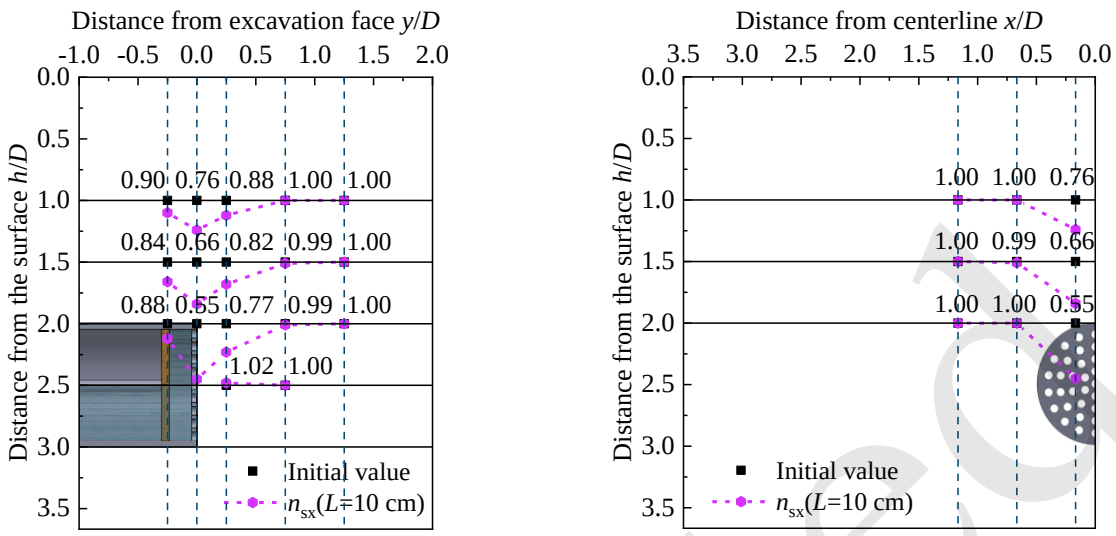

(d)

Fig. 20 The variation rule of n_{sx} with L when α = 0.5: (a) L = 1.5 cm; (b) L = 3 cm; (c) L = 6 cm; (d) L = 10 cm.

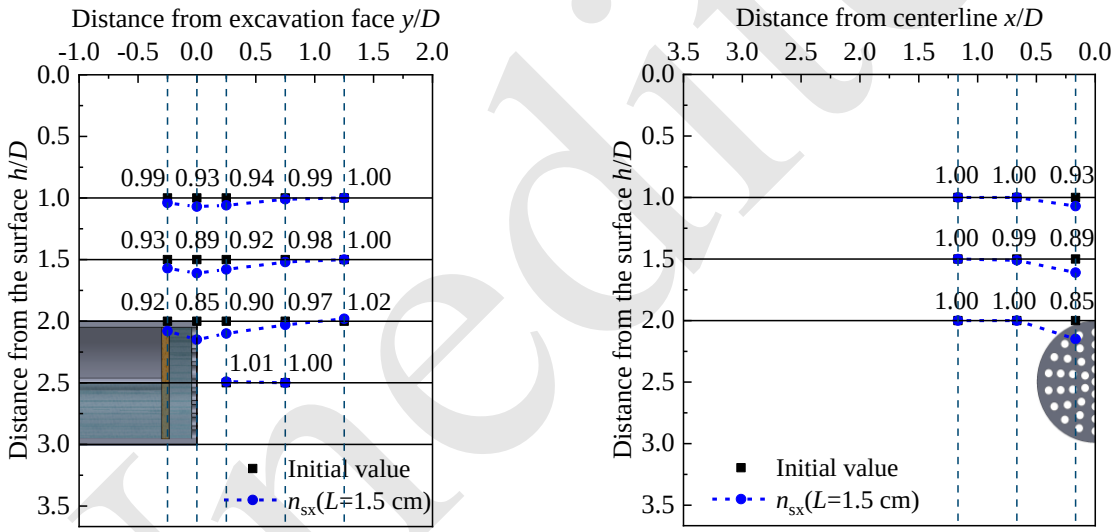

(a)

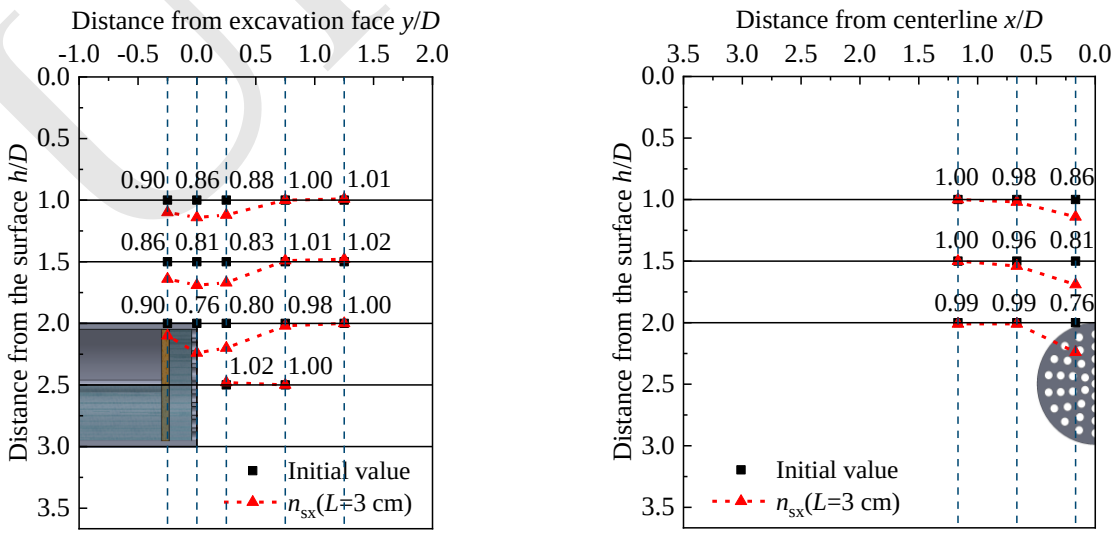

(b)

Unedited

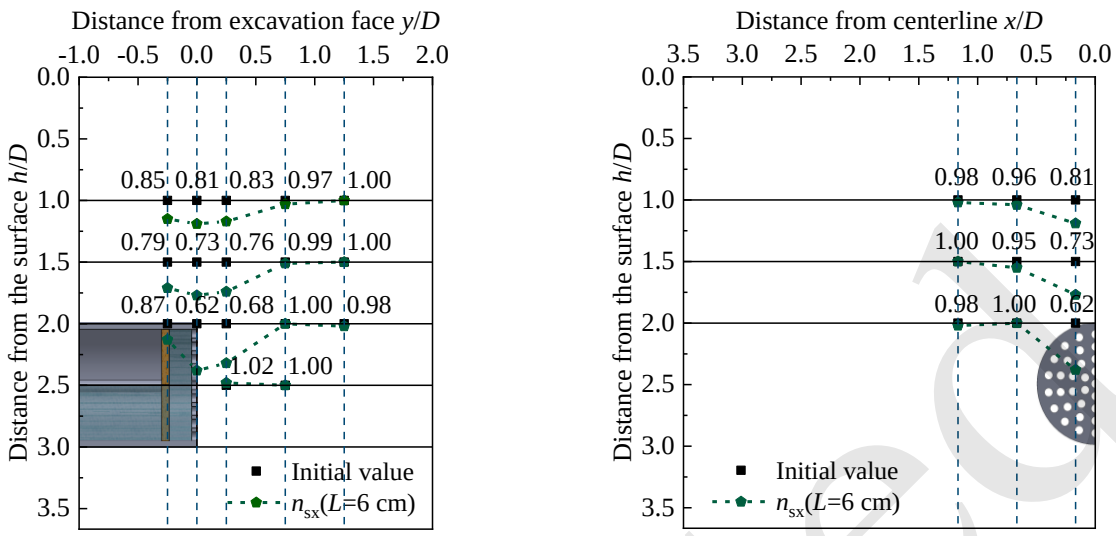

(c)

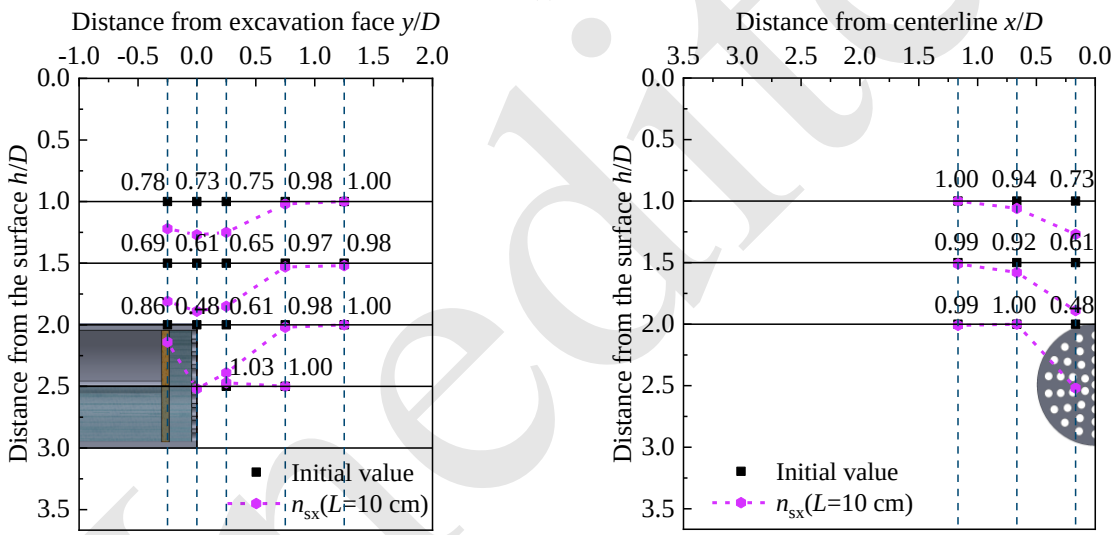

(d)

Fig. 21 The variation rule of n_{sx} with L when α = 0: (a) L = 1.5 cm; (b) L = 3 cm; (c) L = 6 cm; (d) L = 10 cm.

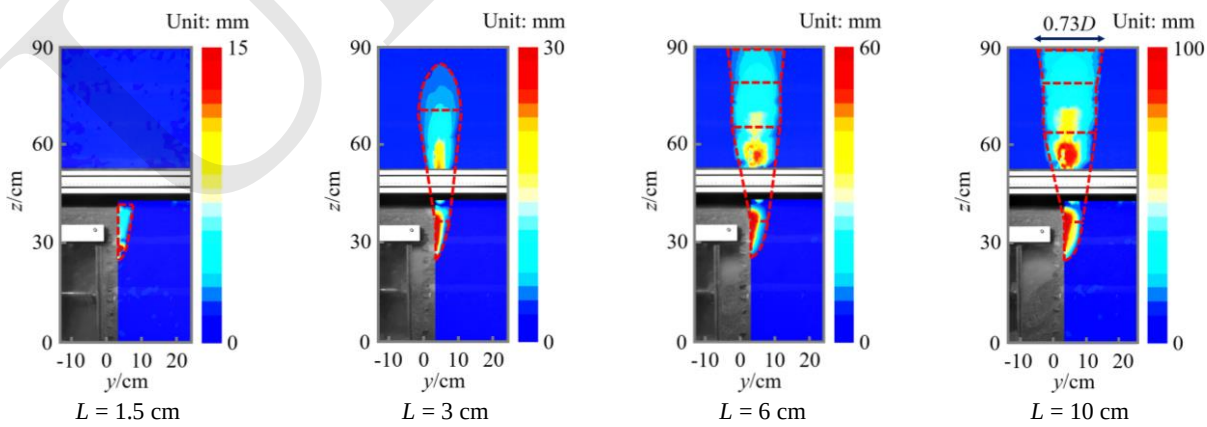

(a)

Unedited

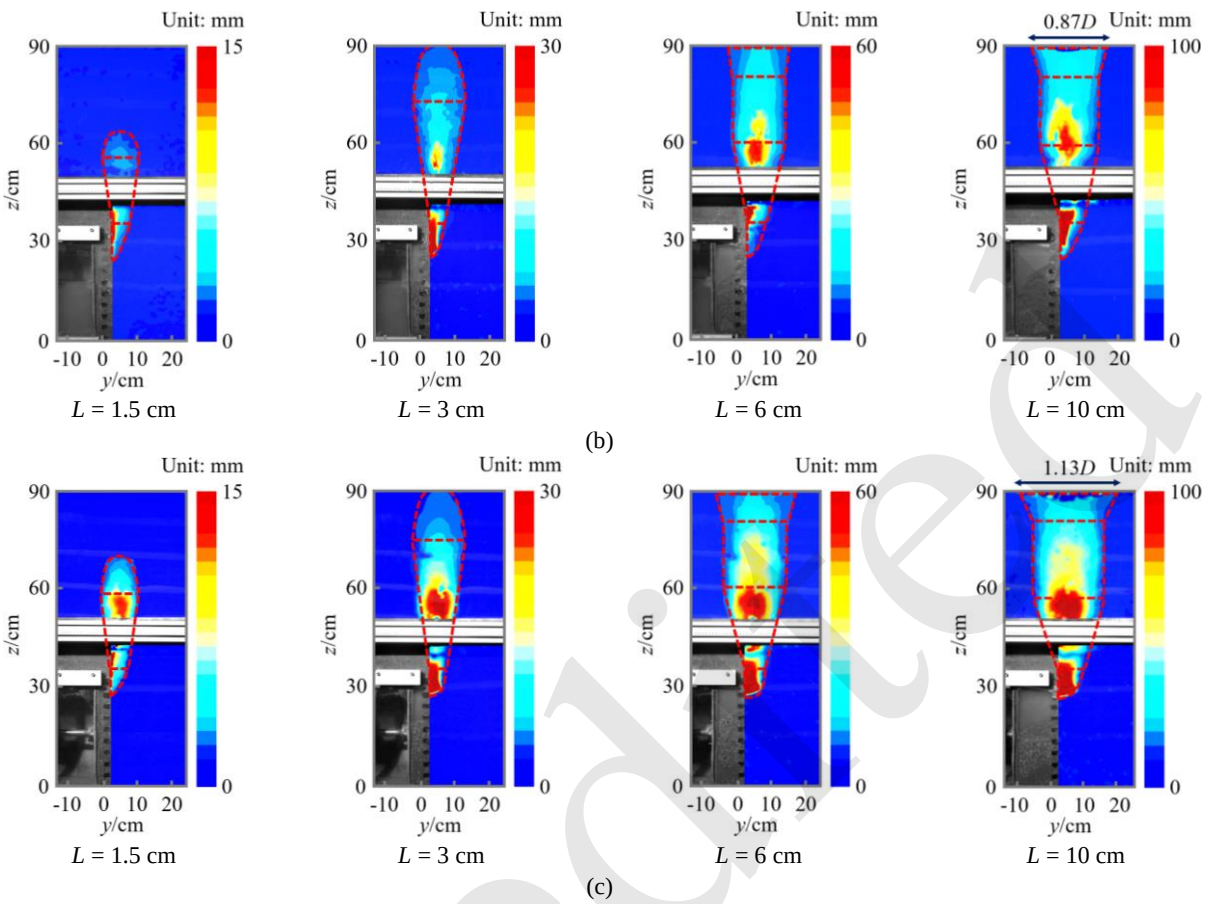

Fig. 22 The instability range of strata for different α values: (a) α = 1; (b) α = 0.5; (c) α = 0.

4.5 Instability range analysis

Looking at Fig. 22, when L = 10 cm, the instability ranges of the strata obtained from numerical simulations under different α values are 0.73D, 0.87D, and 1.13D. Meanwhile, the instability ranges of the strata obtained from numerical simulations are compared with those obtained from the model tests. In Fig. 23, we showcase the instability ranges of the strata under different α conditions for the numerical simulations when L = 10 cm.

The instability ranges of the strata obtained from the numerical simulations for different α values are 0.70D, 0.84D, and 1.06D. The results of the numerical simulations are slightly smaller in value than the results of the model tests. With the decrease of α, the instability range of the strata increases gradually, which is consistent with the conclusions from the model tests.

Meanwhile, the maximum displacement in the strata occurs on the excavation face where the medium dense sandy pebbles are located, which is consistent with the results of the DIC. Differing from the results of the model tests, the excavation face where the dense sandy pebbles are located also deforms, and this is caused by moving the entire excavation face backward in the numerical simulations.

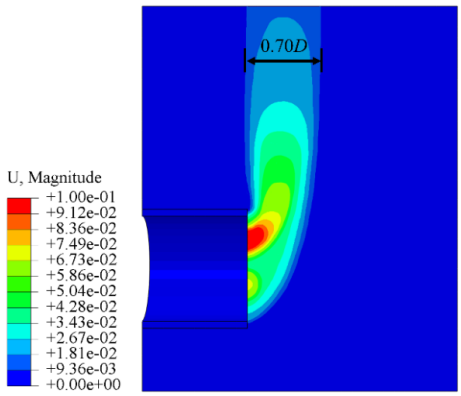

(a)

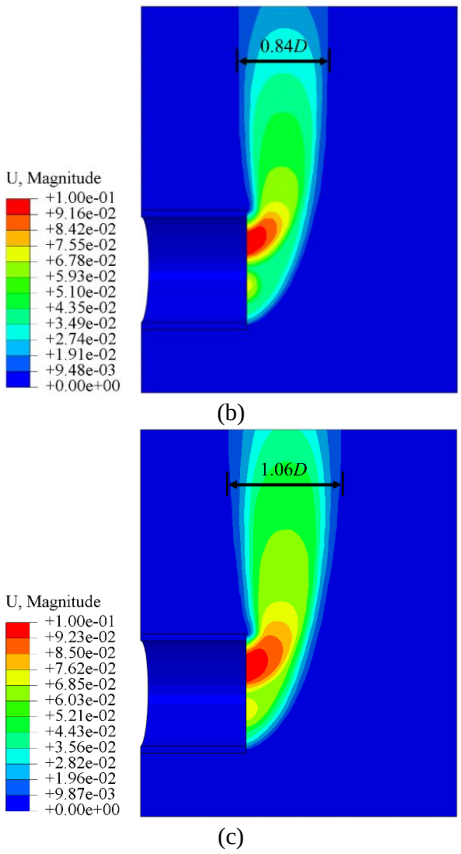

Fig. 23 The instability range of the strata when L = 10 cm for different α values: (a) α = 1; (b) α = 0.5; (c) α = 0.

We point out that Di et al. (2024) used this same model box to study the failure model of an excavation face for water-rich sandy pebble strata, but studied the homogeneous strata with a relative compactness of 0.55. Here we study the failure model of the excavation face for water-rich sandy pebble strata with upper loose and lower dense. Fig. 24 shows the instability ranges of two different strata. When L = 10 cm, except for the homogeneous sandy strata under when α = 1, the overall instability of the homogeneous sandy strata and the sandy pebble strata with upper loose and lower dense have occurred under other conditions. When α changes from 1 to 0, the instability range of the homogeneous sandy strata changes from 0.5D to 1D, while the instability range of the sandy pebble strata with upper loose and lower dense changes from 0.73D to 1.13D. With the decrease of α, the instability range of the two different strata increases. Under the same α value, the instability range of the sandy pebble strata with upper loose and lower dense is larger than that of the homogeneous sandy strata with a relative compactness of 0.55. This is due to the structural discontinuity of the strata with upper loose and lower dense, resulting in uneven stress and deformation at the interface, which can easily cause local instability. Meanwhile, the upper stratum is relatively loose, which produces greater stratum deformation, thus increasing the instability range.

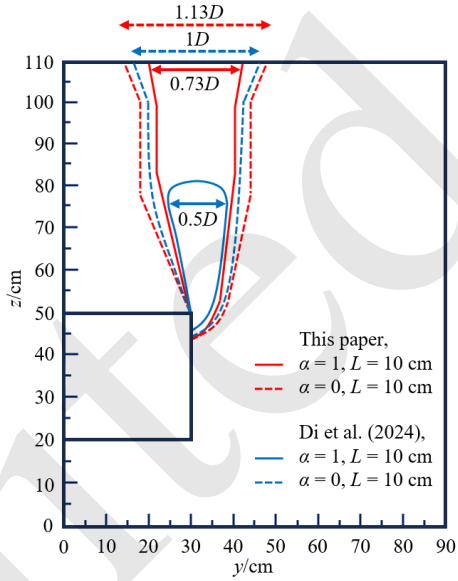

Fig. 24 Comparison of the instability ranges for two different strata.

5 Conclusions

Active instability model tests of excavation face under different α conditions are carried out for water-rich sandy pebble strata with upper loose and lower dense. The following conclusions are obtained from the research.

(1) For varying α conditions, the variation rule of peak displacement of surface settlement with L is categorized into three phases: the non-displacement phase, slow descent phase, and rapid descent phase. After the tests, the surface forms a symmetrical semi-funnel-shaped settlement, whose radius and maximum settlement increase as α decreases.

(2) Under the condition that α = 0.5, the seepage path is within the range of 0-0.53D. And when α = 0, the seepage path is within the range of 0-0.8D. With the decrease of α, the seepage path range will increase, which is consistent with the results obtained from the numerical simulations.

(3) The decrease of α will break the limit equilibrium state of the strata faster, cause early defor-

Unedited

mation and displacement of the soil, and lead to a more rapid alteration in earth pressure on the cutterhead.

(4) With the decrease of α, the disturbed range of earth pressure in the strata becomes larger, which also signals an increase in the instability range of the strata. Moreover, with the increase of L, there is a gradual reduction in earth pressure at various locations within this disturbed range, and this trend becomes more pronounced with smaller values of α.

Acknowledgments

The authors gratefully acknowledge the financial support provided by the National Natural Science Foundation of China (No. 51978019) and Natural Science Foundation of Beijing Municipality (No. 8222004).

Author contributions

Pengfei LI and Chuang WANG designed the research. Chuang WANG processed the corresponding data and wrote the first draft of the manuscript. Xiaopu CUI helped to organize the manuscript. Qing XU, Zhaoguo GE and Shaohua LI revised and edited the final version.

Conflict of interest

Pengfei LI, Chuang WANG, Xiaopu CUI, Qing XU, Zhaoguo GE and Shaohua LI declare that they have no conflict of interest.

References

Chen RP, Yin XS, Tang LJ, et al., 2018. Centrifugal model tests on face failure of earth pressure balance shield induced by steady state seepage in saturated sandy silt ground. *Tunnelling and Underground Space Technology*, 81:315-325. https://doi.org/10.1016/j.tust.2018.06.031

Cheng C, Yang H, Jia PJ, et al., 2023. Face stability of shallowly buried large-section EPB box jacking crossing the Beijing-Hangzhou Grand Canal. *Tunnelling and Underground Space Technology*, 138:105200. https://doi.org/10.1016/j.tust.2023.105200

Cui XP, Li PF, Wu J, et al., 2024. Stability analysis of a shield tunnel in unsaturated soil considering the soil arch effect. *International Journal of Geomechanics*, 24(4):04024041. https://doi.org/10.1061/ijgnai.gmeng-8709

Di QG, Li PF, Zhang MJ, et al., 2022. Analysis of face stability for tunnels under seepage flow in the saturated ground. *Ocean Engineering*, 266:112674. https://doi.org/10.1016/j.oceaneng.2022.112674

Di QG, Li PF, Zhang MJ, et al., 2023a. Influence of permeability anisotropy of seepage flow on the tunnel face stability. *Underground Space*, 8:1-14. https://doi.org/10.1016/j.undsp.2022.04.009

Di QG, Li PF, Zhang MJ, et al., 2023b. Experimental study of face stability for shield tunnels in sandy cobble strata of different densities. *Tunnelling and Underground Space Technology*, 135:105029. https://doi.org/10.1016/j.tust.2023.105029

Di QG, Li PF, Zhang MJ, et al., 2023c. Experimental investigation of face instability for tunnels in sandy cobble strata. *Underground Space*, 10:199-216. https://doi.org/10.1016/j.undsp.2022.10.004

Di QG, Li PF, Zhang MJ, et al., 2024. Experimental study on the effect of seepage flow on the tunnel face stability in the saturated ground. *Ocean Engineering*, 299:117074. https://doi.org/10.1016/j.oceaneng.2024.117074

Fu YB, Zeng DQ, Xiong H, et al., 2022. Seepage effect on failure mechanisms of the underwater tunnel face via CFD-DEM coupling. *Computers and Geotechnics*, 146:104591. https://doi.org/10.1016/j.compgeo.2022.104591

Han KH, Wang L, Su D, et al., 2021. An analytical model for face stability of tunnels traversing the fault fracture zone with high hydraulic pressure. *Computers and Geotechnics*, 140:104467. https://doi.org/10.1016/j.compgeo.2021.104467

He SH, Zhang SC, Li CH, et al., 2017. Blowout control during EPB shield tunnelling in sandy pebble stratum with high groundwater pressure. *Chinese Journal of Geotechnical Engineering*, 39(9):8 (in Chinese).

Hou CT, Yang XL, 2022. 3D stability analysis of tunnel face with influence of unsaturated transient flow. *Tunnelling and Underground Space Technology*, 123:104414. https://doi.org/10.1016/j.tust.2022.104414

Hou CT, Yang XL, Liu MF, et al., 2023. Stability assessment of a non-circular tunnel face with tensile strength cut-off subject to seepage flows: A comparison analysis. *Computers and Geotechnics*, 163:105764. https://doi.org/10.1016/j.compgeo.2023.105764

Hou CT, Pan QJ, Xu T, et al., 2022. Three-dimensional tunnel face stability considering slurry pressure transfer mechanisms. *Tunnelling and Underground Space Technology*, 125:104524. https://doi.org/10.1016/j.tust.2022.104524

Huang MS, Li YS, Shi ZH, et al., 2023. Tunnel face stability model for layered ground with confined aquifers. *Tunnelling and Underground Space Technology*, 132:104916. https://doi.org/10.1016/j.tust.2022.104916

Jiang YF, Zhou P, Zhou FC, et al., 2022. Failure analysis and control measures for tunnel face in water-rich sandy dolomite formations. *Engineering Failure Analysis*, 138:106350. https://doi.org/10.1016/j.engfailanal.2022.106350

Lei HY, Zhang YJ, Hu Y, et al., 2021. Model test and discrete element method simulation of shield tunneling face stability in transparent clay. *Frontiers of Structural and Civil Engineering*, 15(1):147-166. https://doi.org/10.1007/s11709-020-0704-6

Li PF, Cui XP, Xia JW, et al., 2023. Analytical solutions of limit support pressure and vertical earth pressure on cut-

ting face for tunnels. *Underground Space*, 12:65-78. https://doi.org/10.1016/j.undsp.2023.02.004

Li TZ, Dias D, Li ZW, 2020. Failure potential of a circular tunnel face under steady-state unsaturated flow condition. *Computers and Geotechnics*, 117:103231-103231. https://doi.org/10.1016/j.compgeo.2019.103231

Li W, Zhang CP, Tian ZB, et al., 2021. Effect of the seepage flow on the face stability of a shield tunnel. *Tunnelling and Underground Space Technology*, 112:103900. https://doi.org/10.1016/j.tust.2021.103900

Li X, Xue YG, Li ZQ, et al., 2023. Numerical investigation and prediction of the excavation face stability for river-crossing shield tunneling: An intelligent prediction model for limit support pressure. *Computers and Geotechnics*, 160:105493. https://doi.org/10.1016/j.compgeo.2023.105493

Li ZW, Yang XL, Li TZ, 2019. Face stability analysis of tunnels under steady unsaturated seepage conditions. *Tunnelling and Underground Space Technology*, 93:103095-103095. https://doi.org/10.1016/j.tust.2019.103095

Lin QT, Lu DC, Lei CM, et al., 2021. Model test study on the stability of cobble strata during shield under-crossing. *Tunnelling and Underground Space Technology*, 110:103807. https://doi.org/10.1016/j.tust.2020.103807

Liu W, Albers B, Zhao Y, et al., 2016. Upper bound analysis for estimation of the influence of seepage on tunnel face stability in layered soils. *Journal of Zhejiang University-SCIENCE A (Applied Physics & Engineering)*, 17(11):886-902. https://doi.org/10.1631/jzus.A1500233

Lu XL, Zhou YC, Huang MS, et al., 2017. Computation of the minimum limit support pressure for the shield tunnel face stability under seepage condition. *International Journal of Civil Engineering*, 15(6):849-863. https://doi.org/10.1007/s40999-016-0116-0

LüXL, Zhou YC, Huang MS, et al., 2018. Experimental study of the face stability of shield tunnel in sands under seepage condition. *Tunnelling and Underground Space Technology*, 74:195-205. https://doi.org/10.1016/j.tust.2018.01.015

Mi B, Xiang YY, 2020a. Analysis of the limit support pressure of a shallow shield tunnel in sandy soil considering the influence of seepage. *Symmetry*, 12(6):1023. https://doi.org/10.3390/sym12061023

Mi B, Xiang YY, 2020b. Model experiment and calculation analysis of excavation-seepage stability for shallow shield tunneling in sandy ground. *Rock and Soil Mechanics*, 41:837-848 (in Chinese).

Pan QJ, Dias D, 2018. Three dimensional face stability of a tunnel in weak rock masses subjected to seepage forces. *Tunnelling and Underground Space Technology*, 1:555-566. https://doi.org/10.1016/j.tust.2017.11.003

Sohaei H, Hajihassani M, Namazi E, et al., 2020. Experimental study of surface failure induced by tunnel construction in sand. *Engineering Failure Analysis*, 118:104897. https://doi.org/10.1016/j.engfailanal.2020.104897

Tu SQ, Li W, Zhang CP, et al., 2023. Face stability analysis of tunnels in saturated soil considering soil-fluid coupling effect via material point method. *Computers and Geotechnics*, 161:105592. https://doi.org/10.1016/j.compgeo.2023.105592

Wan ZE, Li SC, Zhao SS, et al., 2022. Soil conditioning tests and screw conveyor spewing prevention technology of earth balance pressure shield tunneling in water-rich sandy stratum. *China Civil Engineering Journal*, 55(3):83-93 (in Chinese).

Wang L, Han KH, Xie TW, et al., 2019. Calculation of Limit Support Pressure for EPB Shield Tunnel Face in Water-Rich Sand. *Symmetry*, 11(9):1102-1102. https://doi.org/10.3390/sym11091102

Weng XL, Sun YF, Yan BH, et al., 2020. Centrifuge testing and numerical modeling of tunnel face stability considering longitudinal slope angle and steady state seepage in soft clay. *Tunnelling and Underground Space Technology*, 101:103406. https://doi.org/10.1016/j.tust.2020.103406

Wu J, Li PF, Yao AJ, et al., 2023. Three-dimensional analytical solutions of non-Darcy seepage in front of a grouted subsea tunnel face. *Computers and Geotechnics*, 159: 105509. https://doi.org/10.1016/j.compgeo.2023.105509

Ye Z, Wu H, Wang CX, et al., 2022. Limit face pressure analysis of an EPB shield under suffusion conditions. *Tunnelling and Underground Space Technology*, 130:104733. https://doi.org/10.1016/j.tust.2022.104733

Yin XS, Chen RP, Meng FY, 2021. Influence of seepage and tunnel face opening on face support pressure of EPB shield. *Computers and Geotechnics*, 135:104198. https://doi.org/10.1016/j.compgeo.2021.104198

Zhang SL, Cheng XS, Qi L, et al., 2022. Face stability analysis of large diameter shield tunnel in soft clay considering high water pressure seepage. *Ocean Engineering*, 253:111283. https://doi.org/10.1016/j.oceaneng.2022.111283

Zhang ZH, Xu WS, Nie WT, et al., 2021. DEM and theoretical analyses of the face stability of shallow shield cross-river tunnels in silty fine sand. *Computers and Geotechnics*, 130:103905. https://doi.org/10.1016/j.compgeo.2020.103905

中文概要

题　目：上松下密富水砂卵石地层盾构隧道开挖面稳定模型试验

作　者：李鹏飞[1]，王闯[1]，崔小普[1]，徐晴[1]，葛照国[2]，李少华[3]

机　构：[1]北京工业大学，城市与工程安全减灾省部共建教育部重点实验室，中国北京，100124；[2]中铁十四局集团大盾构工程有限公司，中国南京，211800；[3]中铁十五局集团有限公司，中国上海，200070

目　的：确保水下盾构隧道施工安全的关键环节在于维持开挖面的稳定性，然而目前研究大多针对均质地层，很少针对上部松散下部密实的地层进行开挖面稳定性的研究。本文旨在探讨开挖面的水压比对隧道开挖面稳定性的影响，针对上松下密富水砂卵石地层，进行不同水压比条件下开挖面主动失稳的模型试验研究。

创新点：1. 针对上松下密富水砂卵石地层进行了模型试验；2. 结合 DIC 技术，系统地分析了隧道开挖面的渐进失稳过程。

方　法：1. 通过模型试验，开展不同水压比条件下的开挖面主动失稳试验研究。研究了地表沉降、水压力、刀盘上的土压力和地层中的土压力随挡板后移距离的变化规律；2. 通过数值模拟，建立与模型试验等大的数值模型，数值模拟得到的地表沉降峰值位移、地层失稳范围和渗流路径范围的变化趋势与模型试验的结果一致，验证模型试验结果的准确性。

结　论：1. 在不同的水压比条件下，随着挡板后移距离的增加，地表沉降的峰值位移会经历三个阶段，分别为无沉降阶段，缓慢沉降阶段和快速沉降阶段；2. 水压比的减小，会导致刀盘上土压力的变化更加迅速，并提前引起土体的整体失稳和位移；3. 水压比的减小，会导致水的渗流路径范围和地层的失稳范围增大。

关键词：盾构隧道；上松下密地层；开挖面稳定性；水压比

Unedited